# Fast four-dimensional tensile test monitored via X-ray computed tomography: Elastoplastic identification from radiographs

Clément Jailin, Ante F Buljac, Amine Bouterf, François Hild, Stéphane Roux

# Fast four-dimensional tensile test monitored via X-ray computed tomography: Elastoplastic identification from radiographs

Clément Jailin[1], Ante Buljac[1,2], Amine Bouterf[1], François Hild[1], Stéphane Roux[1]

[1] Laboratoire de Mécanique et Technologie (LMT), ENS Paris-Saclay / CNRS / Univ. Paris-Saclay
61 avenue du Président Wilson, 94235 Cachan (FRANCE)
[2] MINES ParisTech, PSL Research University,
Centre des Matériaux, CNRS UMR 7633, BP 87, 91003 Evry, (FRANCE)

**Abstract**

A Projection-based Digital Image Correlation (P-DVC) method (presented in a companion paper [1]) is extended to an integrated approach for the calibration of an elastoplastic law based on a single radiograph per loading step. Instead of following a two-step sequential procedure (*i.e.,* first, measurement of the displacement field; second, identification), the integrated method aims at identifying few model parameters directly from the gray-level projections. The analysis of an *in-situ* tensile test composed of 127 loading steps performed in 6 minutes is presented. An isotropic elastoplastic constitutive law with free form hardening behavior (*i.e.,* controlled by only 8 parameters) is identified and shows a very ductile behavior (up to 6.3 % strain before failure). A large improvement on the residual quality is shown and validates the proposed model and procedure. The obtained displacement fields revealed to be similar to those measured with no mechanical integration. A different parameterization of the constitutive law provides a very similar result, thereby assessing the robustness of the procedure.

**Keywords:** Tomography; *In-situ* tests; 4D measurement; Inverse methods; Integrated DVC; P-DVC

## 1 Introduction

The identification and validation of increasingly complex mechanical models is a major concern in experimental solid mechanics [2]. Model refinements require ever more precise and complex experimental protocols, from experimental setup and sample (*e.g.,* complex multiaxial loading, optimized geometry) to sensor and acquisition devices (such as infrared, X-ray, or neutron imaging coupled with full field measurements). Especially in 4D situations (*i.e.,* 3D space and time), the acquisition, processing and analysis of such big amounts of data (for the most part redundant) is challenging [3].

Computed Tomography (CT) allows materials to be imaged in 3D, thereby revealing their 3D microstructure in a non-destructive way [4, 5, 6]. Coupled with *ex-situ* or *in-situ* mechanical tests [7, 8, 9, 10], it is possible to measure the deformation of a specimen with full field measurement techniques (Digital Volume Correlation, or DVC [11, 12]) that provide a link with mechanical models and simulations. Intimate experiment-model dialogue has been developed to study crack propagation [13, 14], plastic behavior [15], damage model [16], and allows for model identification and validation [17, 18].

The measured displacement fields are used to calibrate model parameters with inverse methods (*e.g.,* finite element model updating [19], virtual fields method [20]). Because model identification is the final goal of the entire experiment (contrary to displacement fields that are an intermediate step), one may identify and optimize model parameters directly on the acquired images. This fusion of two steps into one, has been called "integrated approach" [15, 21] and leads to a drastic reduction of the number of unknowns. The more loading steps are acquired in the experiment, the more accurate and sensitive the identification procedure. DVC methods have hence been developed in a 4D space-time framework [15, 18, 22] using all available volumes globally. In lab-CT analysis, no more than 10 to 20 acquisitions are usually performed because of the acquisition time (approximately 1 hour is necessary to acquire the 1000 radiographs needed for one full 3D scan).

Projection-based DVC (P-DVC [23]) is a measurement method that aims to measure the 3D displacement fields directly from few radiographs instead of 3D volumes. The outputs of this method are the same as DVC procedures but require two to three orders of magnitude less data, and thus acquisition time. Moreover, the method offers a much enhanced time (or load) resolution from its higher time sampling without significant degradation in spatial resolution, and hence it reveals very valuable in particular for mechanical identification. The comparison between two projections of the sample at the same angle with different loadings can be read as due to 3D motion. Previous works have developed this method for the analysis of a cracked cast iron sample imaged with a synchrotron X-ray source [24, 25]. It was shown that the measurement was possible with only two orthogonal projection angles leading to a huge gain in acquisition time (of a factor 300). The identification of a brittle-elastic behavior of a plaster sample with crack propagation inside of a lab tomograph was performed within such a 4D framework [26].

In a companion paper [1], the measurement of the kinematics from a series of single projections per loading step was presented. Coupling P-DVC and model reduction methods provided a global measurement of the full 4D (*i.e.,* space and time) displacement field. These results will be used as comparison means of the present approach. It is proposed in this paper to identify an elastoplastic model based on a fast 4D measurement. A standard approach would consist of performing the identification from the previously measured displacement fields, using for instance Finite Element Model Updating (FEMU) or the virtual fields method (VFM). In comparison with this pathway, it is shown that the fast 4D kinematic measurement and the identification can be performed in a unique "integrated" procedure, leading to more accurate determination of the constitutive parameters. A free

form representation of the hardening behavior is chosen and controlled by 8 parameters. A variant with 7 parameters leads to a very similar hardening response showing the robustness of the procedure. The test case that was chosen in the companion paper for the kinematic measurements [1] is further analyzed herein. A nodular graphite cast iron dog bone sample was tested *in-situ* with 127 uninterrupted loading steps performed in 6 minutes until failure (leading to a gain in acquisition time of more than 2 orders of magnitude compared to standard methods).

## 2 *In-situ* mechanical test

The main features of the test are summarized hereafter. The interested reader will find additional details in Ref. [1]. The tested sample was made of nodular graphite cast iron (similar to those studied in Refs. [15, 17, 27]). It was tested in uniaxial tension with a slender dog-bone geometry. An *in-situ* tensile testing machine similar to that of Buffière *et al.* [28] was used. The sample was scanned in a lab-tomograph (X-View X50-CT, North Star Imaging, 180 kV, 130 µA, W target, North Star Imaging, Rogers (MN), USA). The voxel size (using $4\times4$ binning at the acquisition stage) was set to 10.7 µm. Each radiograph was averaged with 5 frames in order to reduce acquisition noise without loosing too much time. The radiographs of initial definition $954\times768$ pixels were cropped to a region of interest of $954\times432$ pixels. This set of data will be referred to as "scale 1" in the following. Radiographs were further coarsened by a factor of 2 in all directions (referred to as "scale 2") for speed up. Reconstructions and projections were performed with the ASTRA toolbox [29] with Feldkamp-Davis-Kress (FDK) procedure [30]. The initial projections $f(\boldsymbol{r},\theta)$ could be compared with the re-projection $\Pi_\theta[F(\boldsymbol{x})](\boldsymbol{r})$ of the reconstructed volume $F(\boldsymbol{x})$. The SNR of these projection residuals is 21.7 dB.

A 3D scan of the reference state (subjected to a small load of 250 N in order to remove the backlash that would introduce large rigid body motions) was first acquired. It consisted of 600 radiographs captured at equally spaced angles ranging over a full 360° revolution. The initial force was measured during the procedure (hence considered in the following stress measurement) but the initial elastic deformations of the sample, assumed to be very small were not considered in the displacement measurement. This scan was acquired in 22 min. Then, a continuous rotation of the sample was set with 50 acquisitions per turn. A total of 127 loading steps were acquired over 2.5 turns (see Figure 1). A first series (*i.e.,* one full rotation or 50 projections, up to 100 s) was performed at constant load and was used to quantify the uncertainty. A second series (*i.e.,* 77 projections starting at 100 s) were carried out with a continuous load increase (from 250 to 750 N), which was controlled at a constant stroke velocity of 2 µm/s. Figure 1 shows 3 selected projections at different times (steps 90, 110 and 123). The first one (90) is representative of most of the test where the kinematics will be very well captured. The second one (110) corresponds to a more heterogeneous displacement field (strains not yet localized but concentrated in the central section). It is a more difficult case but will be seen to be very well captured. The last one (123), with a very similar load as the second, is at the onset of localized strain

(actually a crack has initiated). The axial force measurement $\kappa$ during the procedure for each radiograph acquisition is shown in Figure 2.

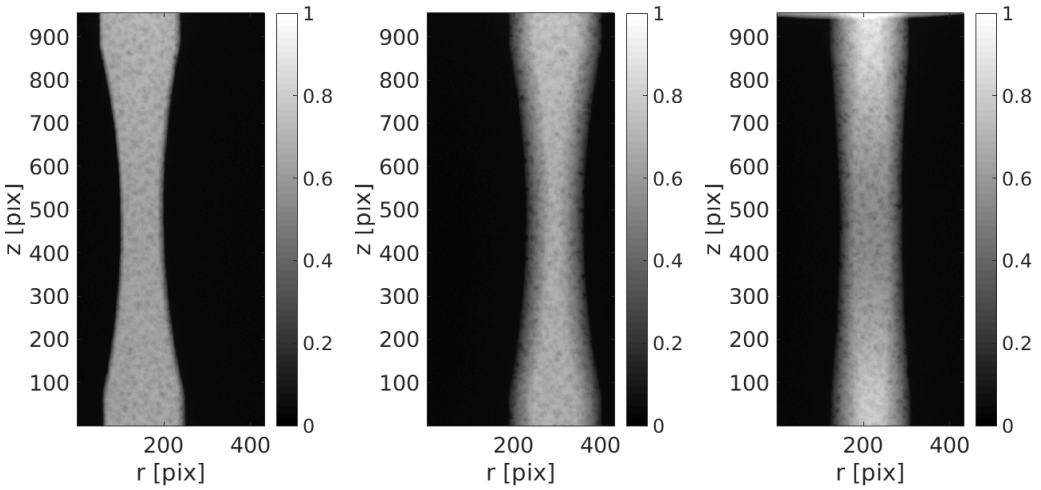


Figure 1: Projection of the sample at different angles and loads during the tensile experiment.(scale 1, where voxel size is equal to 10.7 µm). (a) Time step 90, $\theta = 80°$, $\kappa = 630$ N; (b) time step 110, $\theta = -64.8°$, $\kappa = 715$ N; (c) time step 123, $\theta = -158.4°$, $\kappa = 736$ N

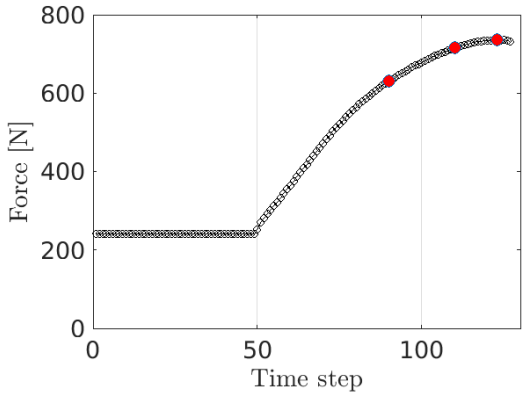


Figure 2: Applied force at steps of the tensile testing machine starting from 250 N. A first rotation is performed at constant load (corresponding to the first plateau up to time step 50, or 100 s) then the load is increased until failure. The three red dots are the projections at time steps 90, 110 and 123 shown in Figure 1

## 3 Full-field measurement method

The proposed "integrated identification" is performed within the P-DVC framework [23, 25]) that is briefly recalled hereafter. In this approach, a key ingredient is the parame-

terization of the displacement field. The slender geometry of the specimen offers a first simplification to a mostly uniaxial displacement field. When a constitutive law is introduced in this framework, the kinematics is further constrained. From this point on, two strategies for identification can be envisioned:
- either a displacement field exploiting only the geometrical constraints is first determined, and then constitutive parameters are calibrated to fit the measured displacement, through a chosen methodology, here FEMU;
- or the constitutive law is directly used to restrict the space of possible displacements considered in the P-DVC procedure. In this so called "integrated" strategy, the kinematics that is measured is directly parameterized by the constitutive parameters, and hence kinematic measurement and identification are performed in a single operation.
In the sequel, the above listed ingredients are introduced in more details.

### 3.1 Projection-based DVC

The P-DVC framework [23, 25]) aims to evaluate the quantities of interest (be they kinematic or mechanical parameters) directly from the radiographs (*i.e.,* the projection at an angle $\theta(t)$ of the 3D microstructure) acquired at different angles and loadings and not from the reconstructed volumes as in standard DVC methods [11, 12, 31].

The registration consists in finding the appropriate 3D displacement field $\boldsymbol{u}(\boldsymbol{x},t)$ by minimizing the quadratic norm of the residual

$$\chi^2[\boldsymbol{u}] = \sum_{\boldsymbol{r},t} \rho(\boldsymbol{r},t;\boldsymbol{u})^2 \tag{1}$$

where $\rho(\boldsymbol{r},t;\boldsymbol{u})$ is the residual field defined as the differences between $N_\theta$ 2D projections $g(\boldsymbol{r},t)$ of the deformed volume at different angles $\theta(t)$. The procedure makes use of the 3D reference image reconstructed using classical means, which provides for all voxels of the 3D space $\boldsymbol{x} = (x,y,z)$ the local x-ray absorption coefficient, $F(\boldsymbol{x})$. This reference volume, corrected by the displacement $\boldsymbol{u}(\boldsymbol{x},t)$, and projected at orientation $\theta(t)$ should coincide with the acquired projections when the solution is reached. In other words, introducing the reference volume deformed with any arbitrary trial displacement field $\boldsymbol{v}$

$$\widetilde{F}_{\boldsymbol{v}}(\boldsymbol{x}) \equiv F(\boldsymbol{x} - \boldsymbol{v}(\boldsymbol{x},t)) \ , \tag{2}$$

the residual field defined as

$$\rho(\boldsymbol{r},t;\boldsymbol{v}) = \Big(\Pi_{\theta(t)}[\widetilde{F}_{\boldsymbol{v}}]\Big)(\boldsymbol{r},t) - g(\boldsymbol{r},t) \tag{3}$$

with $\Pi_{\theta(t)}$ the projection operator in the $\theta(t)$ direction angle and $\boldsymbol{r} = (r,z)$ the coordinates in the detector space.

The previous summand is linearized considering small displacement field correction $\boldsymbol{\delta u}$ compared to the microstructure correlation length

$$\chi^2[\boldsymbol{u}+\boldsymbol{\delta u}] = \sum_{\boldsymbol{r},t} \Big(\rho(\boldsymbol{r},t;\boldsymbol{u}) - \Big(\Pi_{\theta(t)}[\boldsymbol{\delta u}\cdot\boldsymbol{\nabla}\widetilde{F}_{\boldsymbol{u}}]\Big)(\boldsymbol{r},t)\Big)^2 \tag{4}$$

with $\boldsymbol{\nabla}$ the 3D gradient operator. It is noteworthy that after each evaluation of the displacement corrections $\boldsymbol{\delta u}$ from a known displacement $\boldsymbol{u}^{(n-1)}$ such that $\boldsymbol{u}^{(n)} = \boldsymbol{u}^{(n-1)} + \boldsymbol{\delta u}$, a correction of the volume $\widetilde{F}_{\boldsymbol{u}}(\boldsymbol{x})$ is performed so that the previous equation is used without approximation. The P-DVC framework requires the acquisition of one reference volume in order to compute the correction term. The latter is to be performed ideally in the same conditions as the experiment itself, with or without load. This single (classical) tomographic scan is not challenging and can be acquired for example before launching the experiment, in a static configuration.

In order to validate the proper evaluation of the displacement, one should consider the magnitude of the *residual* field that highlights all projection differences that are not explained by the displacement field (*e.g.,* noise, artifacts of the detector, ill-convergence, model error). Ideally, it should be statistically indistinguishable from noise.

### 3.2 Beam regularization of the kinematics

Different regularization procedures of the displacement field have been introduced in the literature for global DVC methods where the kinematics is expressed on a finite element mesh [32]. Model-based regularizations, called strong regularizations or integrated methods with a reduced basis composed of elementary fields issued from a mechanical mode have been considered [15, 21]. It is proposed, in the same spirit as global DVC, to express the displacement field in a reduced basis where the entire kinematics is controlled by the amplitude, $u_i(t)$, of a few fields whose number is denoted by $N_f$

$$\boldsymbol{u}(\boldsymbol{x}, t) = \sum_{i=1}^{N_f} u_i(t) \boldsymbol{\Phi}_i(\boldsymbol{x}) \tag{5}$$

The chosen reduced basis exploits the slender geometry of the sample that makes it amenable to a beam kinematics description [33]. Because of the slowly varying cross section, it is chosen to parametrize the displacement field by rigid body motions of $N_s$ equally spaced cross-sections, with a linear interpolation of the displacement in between. Because of the uniaxial loading prescribed during the test, a single component of the motion (*i.e.,* axial displacement along the $z$ tensile axis) is sought. Hence the spatial displacements of the beam regularization $\boldsymbol{\Phi}_i(\boldsymbol{x})$ is defined as

$$\boldsymbol{\Phi}_i(\boldsymbol{x}) = p_i(z) \boldsymbol{e}_z \tag{6}$$

where $\boldsymbol{e}_z$ accounts for a uniform translation along the tensile axis and $p_i(z)$ the shape functions selecting a specific section and interpolating between them. If the final residual fields are judged unsatisfactory, additional degrees of freedom could easily be added.

It can be noted that no restriction holds on the number of control sections, nor on the type of axial interpolation, and hence the proposed discretization is very generic and is suited to any slender sample geometry.

### 3.3 Mechanical identification

Because the goal is to identify a mechanical behavior with an integrated method, the unknowns of the displacement field are written considering a constitutive model depending on $N_\gamma$ constitutive parameters, gathered in the column vector $\{\boldsymbol{\gamma}\}$. Knowing the constitutive law, the local cross section and the loading at any time $t$ (and possibly its complete history if needed as for elastoplasticity with unloading), it is straightforward to compute the mean axial displacement at control cross sections, and its incremental variation for a variation $\delta\boldsymbol{\gamma}$ of the constitutive parameters about a reference set $\{\boldsymbol{\gamma}^0\}$ for which the section displacements are $u_i^0(t)$

$$u_i(t) = u_i^0(t) + \Gamma_{ij}(t)\delta\gamma_j \tag{7}$$

where $\Gamma_{ij}$ denotes the kinematic sensitivity associated with each parameter $\gamma_j$.

#### 3.3.1 FEMU identification

Finite Element Model Updating (FEMU) [34, 35, 36] is an identification procedure based on the minimization of the quadratic difference between the experimental measured displacement field $\boldsymbol{u}_i^{\text{exp}}(t)$ for each beam section $i$ (identified for each analyzed section and the computed field from the mechanical model $\boldsymbol{u}_i^c(t,\gamma)$

$$\chi^2_{\text{FEMU}} = \sum_{i,t} \|\boldsymbol{u}_i^{\text{exp}}(t) - \boldsymbol{u}_i^c(t,\gamma)\|^2 \tag{8}$$

Here the most standard FEMU method is presented although a metric different from L2 (rather based on the covariance matrix of the measurement data) would be more appropriate [3], or another identification procedure (*e.g.,* VFM).

The computed model has to be controlled by boundary conditions (generally the displacement field measured on surfaces). In this identification approach, the measured load during the experiment is prescribed and controls the kinematics of the beam. The minimization of the linearized functional with respect to the parameters $\gamma$ leads to

$$\delta\gamma_i = \left[\sum_t \Gamma_{ij}(t)\Gamma_{jk}(t)\right]^{-1} \left(\sum_t \Gamma_{kl}(t)(\boldsymbol{u}_l^{\text{exp}}(t) - \boldsymbol{u}_l^c(t,\gamma^0))\right) \tag{9}$$

The result given by FEMU will be compared with those of the integrated approach based on the gray level images, and is considered as a baseline reference.

#### 3.3.2 Integrated identification

The integrated approach aims at identifying the model parameters directly on the images hence minimizing the following functional

$$\{\boldsymbol{\gamma}^{id}\} = \text{Argmin}_{\{\boldsymbol{\gamma}\}}(\chi^2_{\boldsymbol{u}}(\boldsymbol{x}, T(t), \{\boldsymbol{\gamma}\})) \tag{10}$$

It can be noted that this cost function is similar to the one used in Ref. [1] for the P-DVC procedure, at the exception that the displacement field is now parameterized with

the constitutive parameters directly. The derivative of this functional with respect to $\{\boldsymbol{\gamma}\}$ gives an equation very close to FEMU-U but weighted by the gray level uncertainty of each degree of freedom

$$\{\boldsymbol{\delta}\gamma\} = [\boldsymbol{H}]^{-1}\{\boldsymbol{h}\} \tag{11}$$

where $[\boldsymbol{H}]$ is the "gray level" Hessian of $\chi^2_{\boldsymbol{u}}$ with respect to $\{\boldsymbol{\gamma}\}$, $\{\boldsymbol{h}\}$ the residual vector, and $\{\boldsymbol{\delta}\gamma\}$ the correction vector to the current estimate of the sought parameters. It is convenient to write the projected gray level sensitivity for each degree of freedom of each section (*i.e.,* the projected signature of a small motion for each degree of freedom)

$$S_i(\boldsymbol{r}, t) = \Pi_{\theta(t)}[\boldsymbol{\Phi}_i(\boldsymbol{x}) \cdot \boldsymbol{\nabla} F(\boldsymbol{x})] \tag{12}$$

and the associated matrix components

$$B_{ij}(t) = \sum_{\boldsymbol{r}} S_i(\boldsymbol{r}, t) S_j(\boldsymbol{r}, t) \tag{13}$$

Computing and storing this sparse matrix is one of the longest operations in the procedure. However all the sensitivity fields for all parameters of the model are easily obtained from combinations of these projected 3D gray level sensitivity fields. It follows that

$$H_{ij} = \sum_{t} \Gamma_{im}(t) B_{mn}(t) \Gamma_{jn}(t) \tag{14}$$

and

$$h_j = \sum_{\boldsymbol{r},t} \rho(\boldsymbol{r}, t) \Gamma_{jn}(t) S_n(\boldsymbol{r}, t) \tag{15}$$

Before applying this integrated approach, a first measurement and correction of the Rigid Body Motions (RBMs) is convenient. A 4D analysis based on a regularized space (including RBM) and time evolution is first performed using a Proper Generalized Decomposition approach [1]. Then a first estimate of the displacement field is based on scale 2 measurements, which allow large displacements to be coarsely captured (this scale is particularly focused on the edge alignment of the specimen). When scale 2 has converged, the measured displacement field is doubled and used to initialize scale 1 computations.

# 4 Application

## 4.1 Elastoplastic behavior

This paper aims at identifying an isotropic elastoplastic constitutive law. A "free form" isotropic hardening law is proposed with $N_\gamma = 8$ degrees of freedom to describe a piece-wise linear stress strain curve. Such discrete model can be the input behavior for commercial FE softwares. Contrary to some parametric models (*e.g.,* Ludwik [37], Voce [38] or more complex models [39]) whose parameters may lack sensitivity in the measurement procedure, the chosen free form behavior can be designed for identification purposes according to the analyzed experiment.

The degrees of freedom are chosen to have a fixed stress level (imposed by the applied load and sample geometry) while the corresponding strain level is unknown. The calibrated parameters and their initial values are reported in Table 1. The last parameter is chosen as the ultimate strength of all sections during the test. Therefore it controls all sections with high strain levels (*i.e.,* central part of the sample at the highest load). A linear interpolation, in the $[\sigma, \epsilon]$ space is performed between the control points. Other interpolations have been tested in the procedure (*e.g.,* linear) but show no appreciable difference.

Table 1: Free form hardening law parameterized by 8 control points at predetermined stress values. $\epsilon^i$ denotes the initial values of the strain at those control points. $\epsilon^c$ are the calibrated values.

| Parameters | - | $\gamma_1$ | $\gamma_2$ | $\gamma_3$ | $\gamma_4$ | $\gamma_5$ | $\gamma_6$ | $\gamma_7$ | $\gamma_8$ |
|---|---|---|---|---|---|---|---|---|---|
| $\sigma$ [MPa] | 0 | 235 | 335 | 435 | 525 | 555 | 595 | 605 | 620 |
| $\epsilon^i$ [%] (initialization) | 0 | 0.2 | 0.4 | 0.6 | 0.8 | 1.0 | 1.2 | 1.4 | 1.6 |
| $\epsilon^c$ [%] (identified) | 0 | 0.20 | 0.32 | 0.50 | 1.42 | 1.62 | 4.26 | 5.96 | 6.16 |

Because of a low sensitivity on the elastic part, the analysis focuses on the plastic part (*i.e.,* the first slope of the stress-strain curve will not be interpreted as the Young's modulus). In addition to the 8 unknown parameters that control the elastoplastic behavior, a vertical translation is introduced as an additional degree of freedom that may vary arbitrarily in time. Although the vertical motion had been corrected (with respect to gray level residuals) prior to the identification procedure, this extra freedom allows for a fine tuning of the vertical position without any interference with the mechanical identification.

In order to study the robustness of the identified plastic law with respect to the discretization, another identification based on 7 parameters, at different stress levels, is also performed. The same overall behavior is expected.

### 4.2 Initially corrected residual fields

An initial measurement and correction of all rigid body motions is performed based on the method described in Ref. [1]. The SNR increases very significantly from 9.9 to 25.4. The residual field for the three selected angles is shown in Figure 3 with a diverging color map to highlight positive and negative patterns.

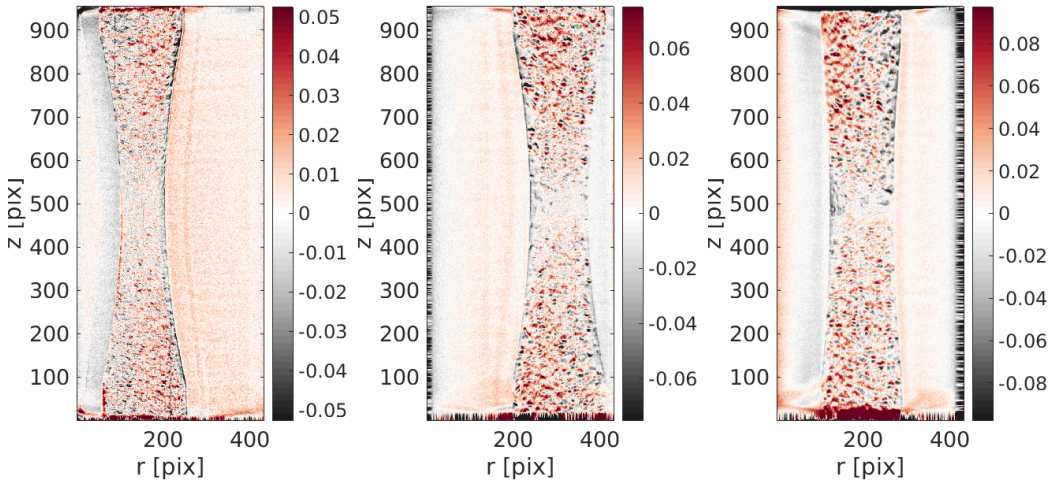


Figure 3: Residual fields from volumes corrected by its rigid body motions. (a) Time step 90, $\theta = 80°$, $\kappa = 630$ N; (b) time step 110, $\theta = -64.8°$, $\kappa = 715$ N; (c) time step 123, $\theta = -158.4°$, $\kappa = 736$ N

With this first procedure, the mean displacement field is corrected and hence the motion appears to be well corrected in the center of the specimen, *i.e.,* the top (resp. bottom) part is moving upward (resp. downward). Alternating positive and negative spots are visible on the top and bottom parts, which are signature of a vertical motion of the sample. Those residuals will be corrected by the following procedure. Note that the color bar amplitudes differ in the figures as they are adapted to the residual amplitude.

### 4.3 Results of the integrated approach

From the initial guess of parameters (shown in Table 1), the procedure aims to identify the set of parameters that leads to the residual field having the lowest norm. The procedure converges in 5 to 7 iterations. A new set of parameters is found (Table 1). The values of the parameters have significantly changed with respect to their initial guess. This result shows that even though the initialization was very far from the converged solution, it did not prevent the algorithm to find a good solution (*i.e.,* the gray level residuals were significantly reduced).

This new set of parameters leads to a mean value of the SNR of 26.4 (the SNR for each radiograph is shown in Figure 4, curve (b)). A decrease of the residuals (*i.e.,* increase of the SNR) is observed from step 80 on, where the displacement correction is large because of plastic yielding. The SNR decreases at the end of the loading (120) step where the model may not be adapted (*i.e.,* high strains including localized features such as necking and shear bands). Low SNRs are located every 25 time steps and correspond to angles where the sample edges are "aligned" with the X-ray beam (*i.e.,* where the residual field is very sensitive to the radial positioning). A very small mis-positioning of the sample generates

large residuals. The small SNR at step 50 is due to the first load increase that may have generated spurious vibrations.

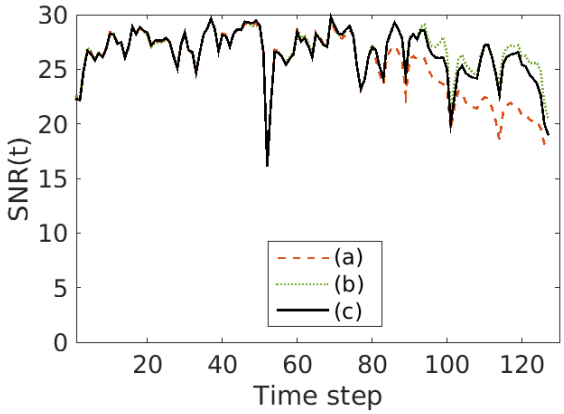


Figure 4: SNR for all radiographs of the test with different corrections. (a) Initial RBM-corrected residual fields, (b) residual fields with the kinematic measurement performed in Ref. [40], (c) at the end of the proposed integrated approach

Figure 5(a) shows the identified mechanical behavior of the studied sample using 3 different procedures (*i.e.,* FEMU and Integrated P-DVC for the 8-parameter hardening law and Integrated P-DVC with the 7-parameter variant). The positions of the control points in the stress space were selected at will, which allowed the hardening curve to be refined where needed. The three approaches lead to very similar shapes especially for the higher strain part, which also corresponds to a high displacement sensitivity after integration of the strain. The difference between 7 and 8 control points (blue and black curves) is minimal, which means that the procedure is not much sensitive to the chosen discretization. These three results are very different from the initial guess, which proves the robustness of the proposed framework. The equivalent stress-strain curve shows a ductile behavior with a total strain reaching approximately 6.3 % in the central part. The longitudinal space-time displacement field obtained from the identified model is shown in Figure 5(b). A displacement amplitude of 16 voxels ($\approx$ 170 µm) is reached at the end of the experiment. High gradients appear in the central part, as expected from the geometry.

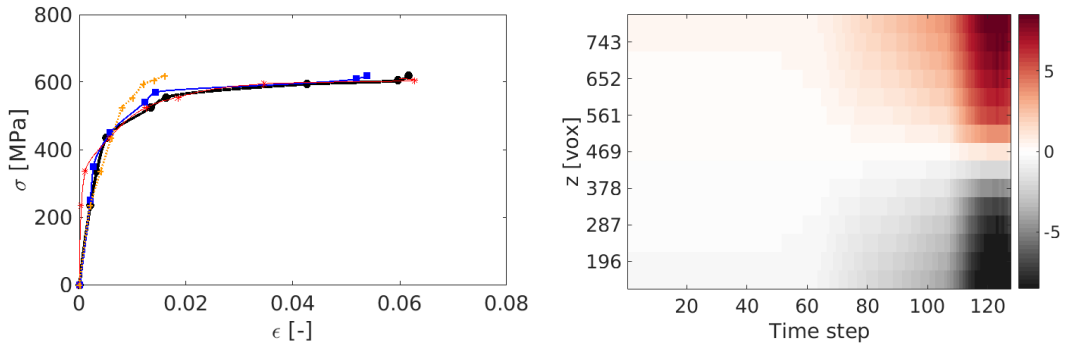


(a) (b)

Figure 5: (a) Equivalent stress-strain curve reconstructed from the converged parameters with different methods. (+, orange): initial guess, (*, red): FEMU approach from displacement results of Ref. [1], (■, blue): integrated approach with 7 unknowns, (•, black): integrated approach with 8 unknowns. (b) Longitudinal displacement expressed in voxels (1 voxel↔ 10.7 µm), obtained from the identification of the mechanical law with the integrated approach with 8 parameters

The residual fields at the end of the analysis are presented in Figure 6. Most of the previous patterns have been erased. Some residuals are still visible in the bottom part of the sample, especially at the end of the experiment and may be due to the localization of plastic strain and/or damage inducing softening. This interpretation is supported by a thin transverse mark at mid-height of the sample ($z \approx 500$ pixels) at the end of the experiment that is visible in Figure 6(c) and may be interpreted as damage localization. This is also consistent with the fact that failure took place at the next scheduled radiograph. The onset of this localized strain band could be traced back to time step 115 where a degradation of the SNR was detected. Although such a phenomenon may occur in reality, as it leads to a breakdown of uniqueness in the solution [41, 42, 43, 44], this situation was excluded from the scope of identification, and the absence of softening was enforced in the parametrization of the constitutive law.

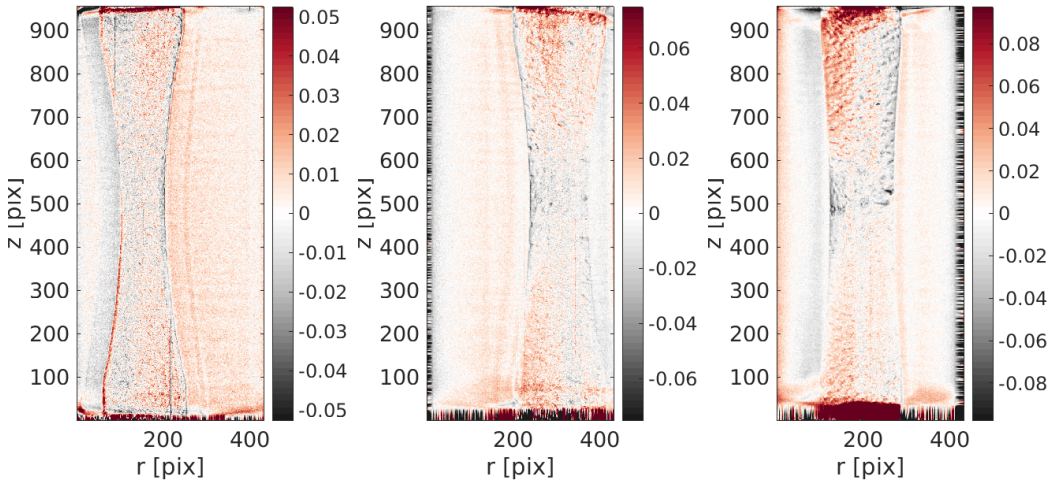


Figure 6: Residual fields from volumes corrected with the identified plastic law. (a) Time step 90, $\theta = 80^o$, $\kappa = 630$ N; (b) time step 110, $\theta = -64.8^o$, $\kappa = 715$ N; (c) time step 123, $\theta = -158.4^o$, $\kappa = 736$ N

## 5 Comparison with kinematic measurements

A comparison with the results obtained in Ref. [1] is performed. A first point is that the SNR whose mean value is 26.4 for the integrated approach and 26.3 with FEMU, is barely smaller than that obtained from the kinematic measurement, namely, 26.7. The temporal changes of the SNR with the two approaches are shown in Figure 4, curves (b-c). Even though it is obtained with a significantly larger amount of degrees of freedom the kinematic approach has only slightly lower residuals. The accuracy of the plastic model based on no more than 7 or 8 parameters is remarkable.

A second comparison has already been performed with the FEMU procedure using the measured displacement field of Ref. [1]. The equivalent stress-strain curve is extremely close to the integrated identification (the first two degrees of freedom are different but they correspond to low displacement sensitivities). The two approaches lead to results that can hardly be distinguished.

The relevance of the chosen model can also be judged from the difference in the identified displacement field. The latter is reported in Figure 7. The mean of the absolute differences is 0.37 voxel and the standard deviation is equal to 0.56 voxel. The low spatial frequency differences are due to model differences (*i.e.,* the identified integrated displacement cannot reproduce the localized behavior).

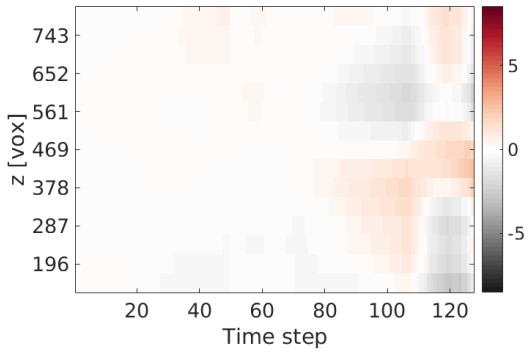


Figure 7: Difference between the displacement field obtained from the integrated approach and that measured with the kinematic approach of Ref. [1]. The color bar is expressed in voxels (1 voxel $\leftrightarrow$ 10.7 µm).

The comparison of the two displacement fields is presented here to show a visual appreciation of the correspondence. It cannot be considered as a judgment criterion of the methods as none of the two fields can be considered as the reference since they are built on different kinematic bases. The only objective comparison metric is given by the gray level residuals [3, 17].

## 6 Conclusion and Perspectives

An integrated method was developed within the Projection Based Digital Volume Correlation framework. Relying on a free form isotropic hardening model, the identification was carried out from radiographs (*i.e.,* 127 projections of the 3D microstructure) instead of 3D (reconstructed) volumes. An *in-situ* tensile test on a spheroidal graphite cast iron sample, where the acquisition was performed on the fly (*i.e.,* with continuous rotation of the sample inside of the tomograph and a continuous loading history until failure) was used to illustrated the identification strategy.

As in the purely kinematic study [1], this approach enabled for huge gains in acquisition time (about 2.5 orders of magnitude as compared to standard approaches). However, the main benefit of the integrated approach is that its outputs consist of the numerical estimate of the constitutive parameters, together with a mechanically admissible displacement field. In the studied example, the calibrated constitutive law was shown to be in good agreement with the one that results from a FEMU procedure applied to the kinematics measured with P-DVC (*i.e.,* with no mechanical constraints). In fact, the integrated approach can be shown to be "optimal" with respect to noise robustness. Additionally, the restriction of the kinematic space to mechanically admissible displacement fields provides a better conditioning of the DVC problem itself, thereby allowing a fine discretization of the kinematics to be used.

A key property of the proposed approach is that the quality of the result can be objectively assessed from the projection residual fields. The identification procedure showed

an important decrease of its norm. A large part of the residual fields was erased with the kinematic correction, meaning that motions were well captured by the model and this observation validated the proposed constitutive law. The onset of strain localization and crack formation can be read from the late residuals, which is a clear demonstration of the ability offered by this tool to either validate a material model, or detect model errors. Moreover, the pathway to correcting the model can often be interpreted from those residuals.

## 7 Acknowledgement

This work has benefited from the support of the French "Agence Nationale de la Recherche" through the "Investissements d'avenir" Program under the reference ANR-10-EQPX-37 MATMECA and ANR-14-CE07-0034-02 COMINSIDE projects.

## References

[1] C. Jailin, A. Buljac, A. Bouterf, F. Hild, and S. Roux. Fast four-dimensional tensile test monitored via X-ray computed tomography: Single projection-based digital volume correlation dedicated to slender samples. *The Journal of Strain Analysis for Engineering Design*, DOI: 10.1177/0309324718797765, 2018.

[2] M. Grédiac and F. Hild, editors. *Full-Field Measurements and Identification in Solid Mechanics*. ISTE / Wiley, London (UK), 2012.

[3] J. Neggers, O. Allix, F. Hild, and S. Roux. Big data in experimental mechanics and model order reduction: Today's challenges and tomorrow's opportunities. *Archives of Computational Methods in Engineering*, 25(1):143–164, 2018.

[4] E. Maire. On the application of X-ray microtomography in the field of materials science. *Advanced Engineering Materials*, 3(8):539–546, 2001.

[5] L. Salvo, P. Cloetens, E. Maire, S. Zabler, J.J. Blandin, J.Y. Buffière, W. Ludwig, E. Boller, D. Bellet, and C. Josserond. X-ray micro-tomography an attractive characterisation technique in materials science. *Nuclear instruments and methods in physics research section B: Beam interactions with materials and atoms*, 200:273–286, 2003.

[6] L. Salvo, M. Suéry, A. Marmottant, N. Limodin, and D. Bernard. 3D imaging in material science: Application of X-ray tomography. *Comptes Rendus Physique*, 11(9):641–649, 2010.

[7] J. Desrues, R. Chambon, M. Mokni, and M.F. Mazerolle. Void ratio evolution inside shear bands in triaxial sand specimens studied by computed tomography. *Géotechnique*, 46(3):529–546, 1996.

[8] A. Guvenilir, T.M. Breunig, J.H. Kinney, and S.R. Stock. Direct observation of crack opening as a function of applied load in the interior of a notched tensile sample of AlLi 2090. *Acta materialia*, 45(5):1977–1987, 1997.

[9] F. Beckmann, R. Grupp, A. Haibel, M. Huppmann, M. Nöthe, A. Pyzalla, W. Reimers, A. Schreyer, and R. Zettler. In-Situ Synchrotron X-Ray Microtomography Studies of Microstructure and Damage Evolution in Engineering Materials. *Advanced Engineering Materials*, 9(11):939–950, 2007.

[10] E. Maire and P.J. Withers. Quantitative X-ray tomography. *International materials reviews*, 59(1):1–43, 2014.

[11] T.S. Smith, B.K. Bay, and M.M. Rashid. Digital volume correlation including rotational degrees of freedom during minimization. *Experimental Mechanics*, 42(3):272–278, 2002.

[12] B.K. Bay, T.S. Smith, D.P. Fyhrie, and M. Saad. Digital volume correlation: three-dimensional strain mapping using X-ray tomography. *Experimental mechanics*, 39(3):217–226, 1999.

[13] J. Rannou, N. Limodin, J. Réthoré, A. Gravouil, W. Ludwig, M.C. Baïetto, J.Y. Buffière, A. Combescure, F. Hild, and S. Roux. Three dimensional experimental and numerical multiscale analysis of a fatigue crack. *Computer Methods in Applied Mechanics and Engineering*, 199:1307–1325, 2010.

[14] H. Toda, E. Maire, S. Yamauchi, H. Tsuruta, T. Hiramatsu, and M. Kobayashi. In situ observation of ductile fracture using X-ray tomography technique. *Acta Materialia*, 59(5):1995–2008, 2011.

[15] F. Hild, A. Bouterf, L. Chamoin, H. Leclerc, F. Mathieu, J. Neggers, F. Pled, Z. Tomičević, and S. Roux. Toward 4D Mechanical Correlation. *Advanced Modeling and Simulation in Engineering Sciences*, 3(1):17, 2016.

[16] L. Babout, E. Maire, and R. Fougeres. Damage initiation in model metallic materials: X-ray tomography and modelling. *Acta Materialia*, 52(8):2475–2487, 2004.

[17] A. Buljac, M. Shakoor, J. Neggers, M. Bernacki, P.-O. Bouchard, Lukas Helfen, T.F. Morgeneyer, and F. Hild. Numerical validation framework for micromechanical simulations based on synchrotron 3d imaging. *Computational Mechanics*, 59(3):419–441, 2017.

[18] A. Buljac, V.M. Trejo Navas, M. Shakoor, A. Bouterf, J. Neggers, M. Bernacki, P.-O. Bouchard, T.F. Morgeneyer, and F. Hild. On the calibration of elastoplastic parameters at the microscale via x-ray microtomography and digital volume correlation for the simulation of ductile damage. *European Journal of Mechanics - A/Solids*, 72:287–297, 2018.

[19] M. Mostafavi, D.M. Collins, B. Cai, R. Bradley, R.C. Atwood, C. Reinhard, X. Jiang, M. Galano, P.D. Lee, and T.J. Marrow. Yield behavior beneath hardness indentations in ductile metals, measured by three-dimensional computed X-ray tomography and digital volume correlation. *Acta Materialia*, 82:468–482, 2015.

[20] B. Rahmani, E. Ghossein, I. Villemure, and M. Levesque. In-situ mechanical properties identification of 3D particulate composites using the Virtual Fields Method. *International Journal of Solids and Structures*, 51(18):3076–3086, 2014.

[21] A. Bouterf, S. Roux, F. Hild, J. Adrien, E. Maire, and S. Meille. Digital Volume Correlation Applied to X-ray Tomography Images from Spherical Indentation Tests on Lightweight Gypsum. *Strain*, 50(5):444–453, 2014.

[22] A. Bouterf, J. Adrien, E. Maire, X. Brajer, F. Hild, and S. Roux. Identification of the crushing behavior of brittle foam: From indentation to oedometric tests. *Journal of the Mechanics and Physics of Solids*, 98:181–200, 2017.

[23] H. Leclerc, S. Roux, and F. Hild. Projection savings in CT-based digital volume correlation. *Experimental Mechanics*, 55(1):275–287, 2015.

[24] T. Taillandier-Thomas, C. Jailin, S. Roux, and F. Hild. Measurement of 3D displacement fields from few tomographic projections. In *SPIE Photonics Europe*, page 98960. International Society for Optics and Photonics, 2016.

[25] T. Taillandier-Thomas, S. Roux, and F. Hild. A soft route toward 4D tomography. *Physical Review Letters*, 117(2):025501, 2016.

[26] C. Jailin, A. Bouterf, M. Poncelet, and S. Roux. In situ $\mu$ CT-scan Mechanical Tests: Fast 4D Mechanical Identification. *Experimental Mechanics*, 57(8):1327–1340, 2017.

[27] Z. Tomičević, J. Kodvanj, and F. Hild. Characterization of the nonlinear behavior of nodular graphite cast iron via inverse identification–analysis of uniaxial tests. *European Journal of Mechanics-A/Solids*, 59:140–154, 2016.

[28] J.-Y. Buffiere, E. Maire, J. Adrien, J.-P. Masse, and E. Boller. In situ experiments with X ray tomography: an attractive tool for experimental mechanics. *Experimental mechanics*, 50(3):289–305, 2010.

[29] W. Van Aarle, W.J. Palenstijn, J. De Beenhouwer, T. Altantzis, S. Bals, K.J. Batenburg, and J. Sijbers. The ASTRA Toolbox: A platform for advanced algorithm development in electron tomography. *Ultramicroscopy*, 157:35–47, 2015.

[30] L.A. Feldkamp, L.C. Davis, and J.W. Kress. Practical cone-beam algorithm. *JOSA A*, 1(6):612–619, 1984.

[31] S. Roux, F. Hild, P. Viot, and D. Bernard. Three-dimensional image correlation from X-ray computed tomography of solid foam. *Composites Part A: Applied science and manufacturing*, 39(8):1253–1265, 2008.

[32] C. Buljac, A.and Jailin, J.and Taillandier-Thomas T.and Bouterf A.and Smaniotto B. Mendoza, A.and Neggers, and S. Hild, F.and Roux. Digital volume correlation: Review of progress and challenges. *Experimental Mechanics*, 58(5):661–708, 2018.

[33] S.P. Timoshenko. *Strength of Materials*. Krieger Publishing Company (3rd edition), 3rd edition edition, 1976.

[34] K.T. Kavanagh and R.W. Clough. Finite element applications in the characterization of elastic solids. *International Journal of Solids and Structures*, 7:11–23, 1971.

[35] K.T. Kavanagh. Extension of classical experimental techniques for characterizing composite-material behavior. *Experimental Mechanics*, 12(1):50–56, 1972.

[36] J.D. Collins, G.C. Hart, T.K. Hasselman, and B. Kennedy. Statistical identification of structures. *AIAA Journal*, 12(2):185–190, 1974.

[37] P. Ludwik. *Elemente der technologischen Mechanik*. Verlag Von Julius Springer, Leipzig (Germany), 1909.

[38] E. Voce. The relationship between stress and strain for homogeneous deformation. *Journal of the Institute of Metals*, 74:537–562, 1948.

[39] J. Lemaitre and J.L. Chaboche. *Mechanics of Solid Materials*. Cambridge University Press, Cambridge (UK), 1990.

[40] C. Jailin, A. Buljac, A. Bouterf, M. Poncelet, F. Hild, and S. Roux. Self-calibration for lab-$\mu$CT using space-time regularized projection-based DVC and model reduction. *Measurement Science and Technology*, 29(2):024003, 2018.

[41] J.W. Rudnicki and J.R. Rice. Conditions for localization of deformation in pressure-sensitive dilatant materials. *Journal of the Mechanics and Physics of Solids*, 23:371–394, 1975.

[42] J.R. Rice. *The Localization of Plastic Deformations*, pages 207–220. North-Holland, 1976.

[43] R. Billardon and I. Doghri. Prediction of macro-crack initiation by damage localization. *Comptes Rendus de l'Académie des Sciences Paris, série II*, 308(4):347–352, 1989.

[44] G. Borré and G. Maier. On linear versus nonlinear flaw rules in strain localization analysis. *Meccanica*, 24:36–41, 1989.